Chemical Reaction Induced Mass Transport at Surfaces

J. WAYNE RABALAIS

Department of Chemistry, University of Houston, Houston, Texas 77204-5641

Received June 16, 1993

Although it is well-known that atoms at the surface of a solid are mobile, as established by studies of surface diffusion which started more than 70 years ago,[1] the classical concept of a static surface and the question of "Where do atoms sit?" has persisted until recently. As a result of the development of new experimental techniques and theoretical methods, this impression is rapidly evolving into the concept of a dynamically changing surface. Mass transport at surfaces due to surface atom mobility is now recognized as one of the most important stages in many practical processes involving adsorption, desorption, heterogeneous catalysis, crystal growth, etc.

The clean surfaces of many materials are known to exhibit the two-dimensional periodicity of the corresponding bulk planes. Some crystal surfaces spontaneously reconstruct, i.e., the surface atoms are rearranged into a different periodicity, whereas in other crystals such reconstruction can be induced. Adsorbate-induced restructuring of surfaces was originally proposed by Langmuir[2] in 1916. The driving force behind such reconstruction is related to the formation of strong substrate–adsorbate bonds relative to substrate–substrate bonds. When a chemisorbed system has a high enthalpy of adsorption, the thermodynamic driving force is often sufficient to induce relocation of both substrate and adsorbate atoms for formation of an ordered stable surface compound. Several excellent reviews[3] describing developments and aspects of reconstruction, adsorbate-induced reconstruction, and diffusion are available.

Direct observation of atomic diffusion and rearrangement on surfaces has become possible through modern surface science techniques. The field ion microscope[4] is able to monitor random walks of individual atoms or small atomic clusters on the surface of metallic tips. Low-energy electron diffraction (LEED)[5] is capable of recording long range order (coherence length $\approx$ 100–200 Å) adsorbate and substrate symmetry changes in reciprocal space. Scanning tunneling microscopy (STM) and atomic force microscopy (AFM) can directly monitor atomic scale changes in surface electron density in real space.[6] The techniques of glancing angle X-ray diffraction,[7] photoelectron diffraction,[8] and surface extended X-ray adsorption fine structure (SEXAFS)[9] provide information on the phases and interatomic spacings in surfaces. Low-energy (LEIS),[10] medium-energy (MEIS),[11] and high-energy (HEIS)[12] ion scattering measures interatomic spacings in real space in the surface, subsurface, and bulk layers, respectively, of materials. The surface atomic periodicity and interatomic spacings for both adsorbate and substrate atoms can be measured directly by using a LEIS method called time-of-flight scattering and recoiling spectrometry (TOF-SARS).[13,14]

This Account presents an example of the mechanism of an adsorbate-induced reconstruction, along with the inhibition of the process, as delineated by the technique of TOF-SARS. The system chosen to exemplify the chemical reaction induced mass transport and inhibition is that of O_2 chemisorption on a Ni{110} surface with sulfur contamination. Chemisorption of oxygen and sulfur on Ni{110} has been studied extensively. It is well established that, at room temperature, oxygen is dissociatively chemisorbed at the long-bridge sites between first-layer Ni atoms above the ⟨001⟩ rows and that this chemisorption induces reconstruction such that some of the first-layer Ni rows are missing along the ⟨001⟩ direction.[15] The chemisorption site for sulfur has been found to be the 4-fold hollow sites in which S is bonded to four Ni atoms in the surface plane and one Ni atom in second layer.[16] Additional details concerning these structures will be given at the appropriate places in the text.

J. Wayne Rabalais was born in Bunkie, LA in 1944. He obtained his B.S. degree from the University of Southwestern Louisiana in 1966 and his Ph.D. from Louisiana State University in 1970. He was awarded a NATO Postdoctoral Fellowship for research in X-ray and UV photoelectron spectroscopy and Auger spectroscopy at the University of Uppsala in Sweden in 1970–1971. Following this, he joined the faculty at the University of Pittsburgh and then moved to the University of Houston in 1975, where he presently holds the position of Hugh Roy and Lilly Grantz Cullen Professor. His research interests have been in surface science, with emphasis in two areas: (i) development of time-of-flight scattering and recoiling spectrometry as a surface crystallography and (ii) the use of low-energy ion beams for direct deposition of thin films by the subplantation method.

(1) Volmer, M.; Estermann, J. *Z. Phys.* **1921**, *7*, 13.
(2) Langmuir, I. *J. Am. Chem. Soc.* **1916**, *38*, 2221.
(3) Thiel, P. A.; Estrup, P. J. Metal Surface Reconstructions. In *C.R.C. Handbook of Surface Imaging and Visualization*; Hubbard, A. T., Ed.; CRC Press: Boca Raton, FL, in press. Van Hove, M. A. Crystal Surfaces. In *Structure of Solids, Materials Science and Technology*; Gerold, V., Ed.; Verlag Chemie: Weinheim, 1991. Somorjai, G. A.; Van Hove, M. A. *Prog. Surf. Sci.* **1989**, *30*, 201. Estrup, P. J. Reconstruction of Metal Surfaces. In *Chemistry and Physics of Solid Surfaces*; Vanselowe, R., Howe, R., Ed.; Springer-Verlag: Berlin, 1984; p 205.
(4) Muller, E. W.; Tsong, T. T. *Field Ion Microscopy*; American Elseiver: New York, 1969. Tsong, T. T. *Phys. Today* **1993**, *46*, 24.
(5) Hudson, J. B. *Surface Science. An Introduction*, Butterworth-Heinemann: Boston, 1992 and references therein.
(6) Scanning Tunneling Microscopy. In *Methods of Experimental Physics*; Stroscio, J. A., Kaiser, W. J., Eds.; Academic Press, Inc.: Boston, 1993; Vol. 27.
(7) Feldman, L. C.; Mayer, J. W. *Fundamentals of Surface and Thin Film Analysis*; North-Holland: New York, 1986; p 167.
(8) *The Structure of Surfaces III*; Vol. 24, Springer Series in Surface Sciences; Tong, S. Y., Van Hove, M. A., Takayanagi, K., Xie, X. D., Eds.; Springer-Verlag: Berlin, 1991; p 85.
(9) Citrin, P. *J. Phys. (Paris)* **1986**, *47*, C8-437. Reference 7, p 181.
(10) Niehus, H.; Heiland, W.; Taglauer, E. Low Energy Ion Scattering at Surfaces; *Surf. Sci. Rep.* **1993**, *17*, 213.
(11) Parilis, E. S.; Kishinevsky, L. M.; Turaev, N. Yu.; Baklitzky, B. E.; Umarov, F. F.; Verleger, V. Kh.; Bitensky, I. S. *Atomic Collisions on Solids*; North-Holland: New York, 1993.
(12) Reference 7, p 99.
(13) Grizzi, O.; Shi, M.; Bu, H.; Rabalais, J. W. *Rev. Sci. Instrum.* **1990**, *61*, 740.
(14) Rabalais, J. W. *Science* **1990**, *250*, 521.
(15) O'Connor, D. J. *Surf. Sci.* **1986**, *173*, 593. Voiglander, B.; Lehwald, S.; Ibach, H. *Surf. Sci.* **1990**, *225*, 162. Kleinle, G.; Wintterlin, J.; Ertl, G.; Behm, R. J.; Jona, F.; Mority, W. *Surf. Sci.* **1990**, *225*, 171.

0001-4842/94/0127-0026$04.50/0

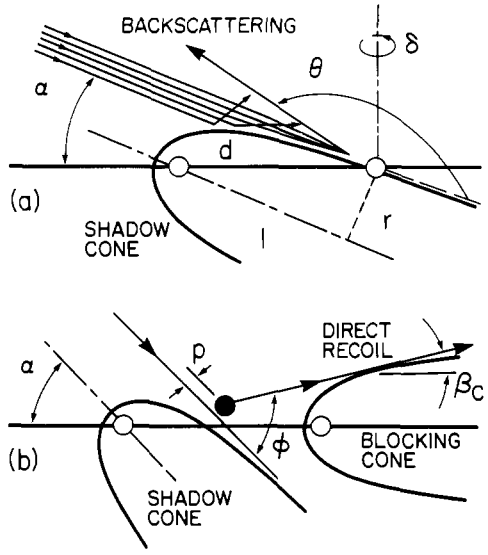

Figure 1. Schematic illustration of scattering with shadowing effects and direct recoil with shadowing and blocking effects. Scattering and recoiling parameters are indicated.

The mechanisms (i) by which chemisorption of 0.2 langmuir (1 langmuir = 10^{-6} Torr·s) of O_2 gas on a Ni{110} surface at room temperature can induce the migration of $\approx 5 \times 10^{14}$ Ni atoms/cm^2 and (ii) by which the presence of 1–3 atom % of sulfur atoms in the surface layers can inhibit this migration will be delineated herein. TOF-SARS is capable of observing the static structures before and after the O_2-induced reconstruction; the presence of sulfur impurities provides the clue to the diffusion path of the Ni atoms. Since oxygen and sulfur can drastically modify the chemical reactivity of Ni, this system carries practical significance in understanding the mechanisms of metal oxidation and heterogeneous catalysis. Specifically, sulfur is known to have deleterious effects on certain catalytic reactions; even very small concentrations of sulfur can poison catalysts for methanation and Fischer–Tropsch reactions.

We begin with a brief description of the TOF-SARS technique, delve into the details of the O_2/Ni system and the influence of sulfur, and then discuss the mechanism of the mass transport.

Time-of-Flight Scattering and Recoiling Spectrometry

Basic Physics Underlying Kiloelectronvolt Ion Scattering and Recoiling. The dynamics of kiloelectronvolt atomic collisions are well described as binary collisions between the incident ion and surface atoms.[17] When an energetic ion makes a collision with a surface atom,[18] the ion is scattered and the surface atom is recoiled into a forward direction as shown in Figure 1. Both the scattered and recoiled atoms have high, discrete kinetic energies which can be calculated from the laws of conservation of energy and momentum.[17] The interatomic interactions can be described by screened Coulomb potentials, for which there are several good models.[17] Such a potential allows determination of the relationship between the scattering θ and recoiling ϕ angles and the impact parameter p of the collision.

Anisotropy Caused by Shadowing and Blocking Cones. Ion trajectories incident on a surface are bent by the repulsive potentials of individual atoms such that an excluded volume, called a *shadow cone*, in the shape of a paraboloid is formed behind the target atom as shown in Figure 1. Ion trajectories do not penetrate into the shadow cone, but instead are concentrated at its edges. Similarly, if the scattered or recoiled atom trajectory is directed toward a neighboring atom, that trajectory will be blocked, resulting in formation of a *blocking cone* behind the neighboring atom into which no particles can penetrate. The cone dimensions can be constructed theoretically[17,19] from the relationship of p with θ and ϕ, they can be obtained from a universal shadow cone curve,[19] or they can be determined experimentally from crystals with known interatomic spacings.[20,21] Since the radii of these cones are of the same order as interatomic spacings, i.e., 1–2 Å, the ions penetrate only into the outermost surface layers. A collimated ion flux impinging on a crystal surface is scattered and recoiled in an anisotropic manner due to the spatial arrangement of atoms in the lattice. For different crystal structures, atomic densities along the various azimuths differ and, hence, the ability of the ions to channel, i.e., to penetrate into empty spaces between atomic rows. The cones determine which nuclei are screened from the impinging ion flux and which exit trajectories are blocked. Measuring the flux of scattering and recoiling atoms as a function of ion beam incident and azimuthal angles enables observation of structures which can be interpreted in terms of the interatomic spacings and shadow cones.

The TOF-SARS Technique. The TOF-SARS technique and instrumentation have been described previously.[13,14] Briefly, a monoenergetic, pulsed, rare-gas ion beam is directed onto a sample, and the scattered and recoiled neutral plus ion flux is velocity analyzed by TOF techniques. Typical experimental parameters are 2–5-keV pulsed He^+, Ne^+, or Ar^+ beam, pulse width $\approx$30 ns, pulse rate $\approx$30 kHz, and average current density $<$0.1 nA/mm^2. A typical TOF spectrum is shown in Figure 2. Peak intensities, obtained by integrating narrow windows centered at the peak maxima, plotted as a function of incident α or azimuthal δ angle exhibit anisotropy as described above. Classical ion trajectory calculations[14] using theoretical models of the surface are used to simulate the TOF-SARS spectra and their angular anisotropy. The shapes of the shadowing and blocking cones determined from these calculations are used to determine the interatomic spacings and surface periodicity, as will be described in detail below. The advantages of TOS-SARS for surface structure studies are that it is element-specific and sensitive to all elements, has first-layer specificity, is sensitive to short-range ($<$10 Å) order, and provides information in real space. Its major disadvantage is the limited mass resolution.

(16) Warburton, D. R.; Thornton, G.; Norman, D.; Richardson, C. H.; McGrath, R. *Surf. Sci.* **1987**, *189/190*, 495. Van Der Veen, J. F.; Tromp, R. M.; Smeenk, R. G.; Saris, F. W. *Surf. Sci.* **1979**, *82*, 468.

(17) Mashkova, E. S.; Molchanov, V. A. *Medium-Energy Ion Reflection From Solids*; North-Holland: Amsterdam, 1985.

(18) Rabalais, J. W. *Crit. Rev. Solid State Mater. Sci.* **1988**, *14*, 319.

(19) Zeigler, J. F.; Biersack, J. P.; Littmark, U. *The Stopping and Range of Ions in Solids*; Pergamon: New York, 1985.

(20) Chang, C. S.; Knipping, U.; Tsong, I. S. T. *Nucl. Instrum. Methods Phys. Res.* **1986**, *B18*, 11; **1988**, *B35*, 151.

(21) Grizzi, O.; Shi, M.; Bu, H.; Rabalais, J. W. *Phys. Rev. B* **1989**, *40*, 10127.

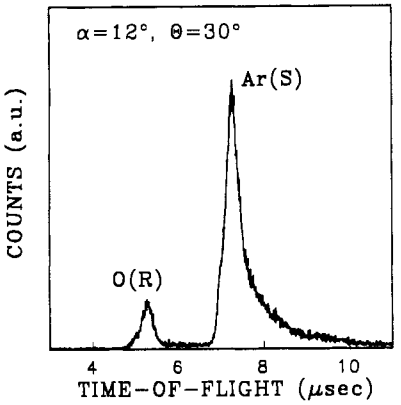

Figure 2. Example of a TOF spectrum from the Ni{110}-(2×1)-O surface. Conditions: 4-keV Ar^+ projectiles; scattering θ and recoiling angles $\phi = 30°$; beam incident angle to surface $\alpha = 12°$ along the $\delta = 0°$ azimuth ⟨001⟩.

Oxygen-Induced Reconstruction of the Ni{110} Surface

Ni–Ni First-Layer Interatomic Spacings. The clean Ni{110} surface is a bulk truncated structure with (1 × 1) atomic periodicity. Oxygen has been found[15] to be dissociatively chemisorbed at the long-bridge sites along the ⟨001⟩ rows. Upon exposure to increasing O_2 dose, the following sequence of LEED patterns develops:[22] an initial streaky $(3\times1)_i$ after 0.2-langmuir exposure, a sharp (2×1) after 0.75 langmuir, and a final sharp $(3\times1)_f$ after 4.0 langmuirs. Incident angle α scans of the Ne scattering intensity I(S) along the ⟨1$\bar{1}$0⟩ azimuth from the clean Ni surface and the three oxygen-induced surface phases[23] are shown in Figure 3A. The critical incident angles α_c are obtained as the α value for which I(S) is 50% of the peak maximum following background subtraction. The interatomic distance d in the scattering plane is calculated directly from α_c, as described elsewhere.[13,14]

For the clean (1×1) phase, $\alpha_c = 15.2°$ for first-layer atoms shadowing neighboring first-layer atoms, in agreement with the lattice spacing of Ni (d = 2.49 Å) as determined by shadow cone analysis. For the $(3\times1)_i$ phase, two shoulders appear at $\alpha < 14°$, indicating the formation of local structures in which the Ni–Ni spacing is longer than in the previous structure. These shoulders at $\alpha_c \approx 6.5°$ and 10° correspond, respectively, to Ni–Ni spacings of ≈7.5 and ≈5.0 Å, i.e., tripling ($3d$) and doubling ($2d$) of the lattice spacings. The 6.5° shoulder disappears in the (2×1) phase, leaving only a sharp rise in I(S) at 10°, corresponding to a $2d$ lattice spacing. For the $(3\times1)_f$ phase, the α_c remains at 10°, the reasons for which will be described below. The α_c values[24] calculated from the shadow cone as a function of Ni–Ni spacing are shown in Figure 3B.

The interatomic spacings determined in Figure 3A are consistent with the structures shown in Figure 4. The $(3\times1)_f$ phase consists of first-layer ⟨001⟩ rows which are separated by 3 times the ⟨1$\bar{1}$0⟩ interatomic spacing; i.e., two rows are absent out of every three first-layer ⟨001⟩ rows. The (2×1) phase consists of first-layer ⟨001⟩ rows which are separated by 2 times the ⟨1$\bar{1}$0⟩ interatomic spacing. The $(3\times1)_f$ phase consists of alternating (2×1) and (1×1) structures; i.e., one row is absent out of every three rows, resulting in $2d$ and d spacings. The α_c corresponding to the d spacings of $(3\times1)_f$ is not resolved from that of the $2d$ spacings at lower α, although it is noted as a sharp rise near 16°.

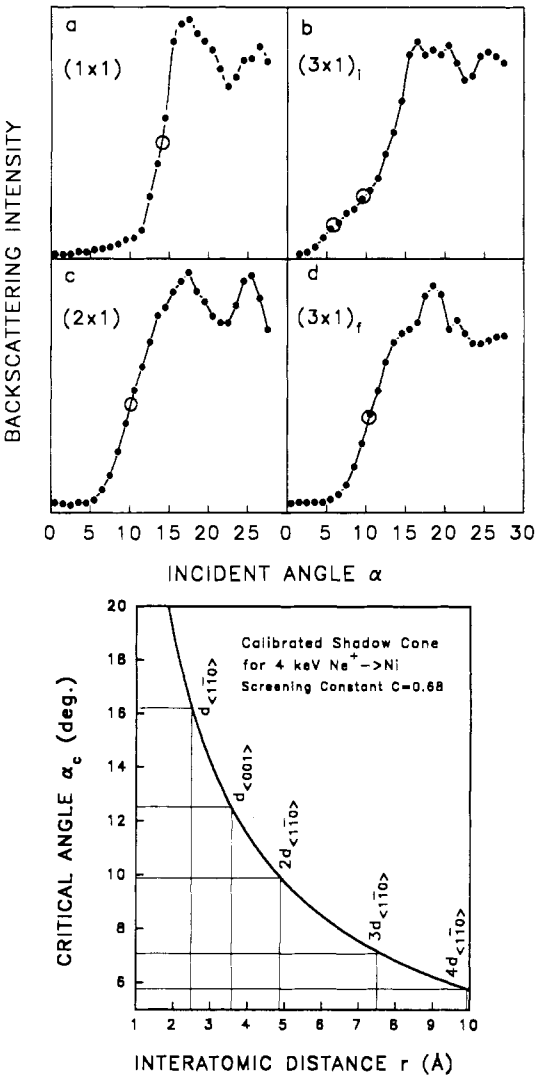

Figure 3. (A) Backscattering intensity I(S) vs incident angle α scans along the ⟨1$\bar{1}$0⟩ azimuth from different phases of Ni{110}: (a) (1×1); (b) $(3\times1)_i$; (c) (2×1); (d) $(3\times1)_f$. The critical incident angles α_c are denoted by large open circles. Scattering angle θ = 90°. (B) Critical incident angle α_c vs Ni–Ni interatomic distance as obtained from shadow cone calculations. The lattice spacings d along the ⟨1$\bar{1}$0⟩ and ⟨001⟩ azimuths and the multiples of these spacings along ⟨1$\bar{1}$0⟩ are indicated.

Ni–Ni First-Layer Periodicity. Azimuthal angle δ scans of the Ne scattering intensity I(S) were carried out in order to expose the principal azimuths along which the neighboring first-layer atoms are aligned.[23] Such scans for the clean (1×1) and the oxygen-induced (2×1) and $(3\times1)_f$ phases are shown in Figure 5; the streaky $(3\times1)_i$ phase was not attempted because it consists of a mixture of the $(3\times1)_i$ and (2×1) phases, as will be shown below. The minima observed in Figure 5 correspond to the azimuthal directions along which first-layer atoms are aligned. The widths W of the minima along specific azimuths increase as the interatomic spacings along that azimuth decrease because of the larger δ rotation required for the neighboring atoms to move out of the shadow cones. These widths increase in the order $W_{(1\times1)} > W_{(3\times1)f} > W_{(2\times1)}$ along the

(22) Demuth, J. E. *Colloid Interface Sci.* **1977**, *58*, 184. MacRae, A. U. *Surf. Sci.* **1964**, *1*, 319. Masuda S.; Nishijima, M.; Sakisaka, Y.; Onchi, M. *Phys. Rev. B* **1982**, *25*, 863.
(23) Bu, H.; Roux, C. D.; Rabalais, J. W. *J. Chem. Phys.* **1992**, *97*, 1465.
(24) Roux, C. D.; Bu, H.; Rabalais, J. W. *Chem. Phys. Lett.* **1992**, *200*, 60.

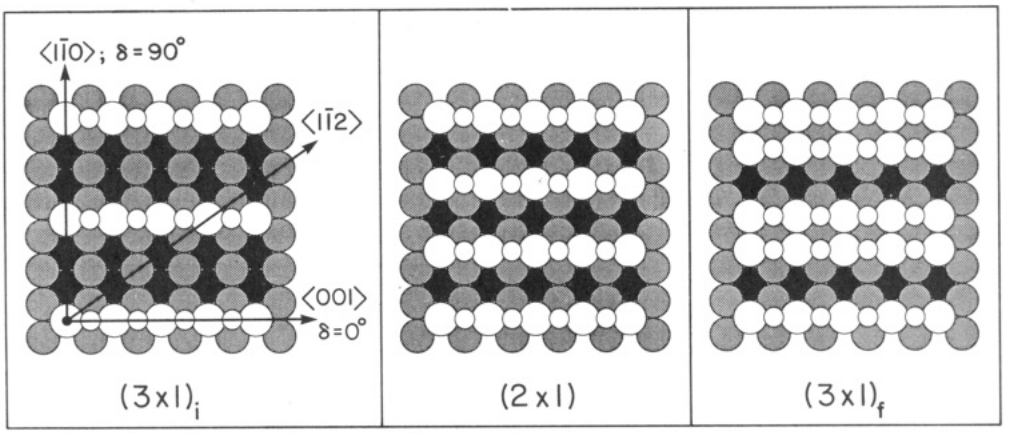

Figure 4. Top view of the three different phases of a Ni{110} surface after various O_2 exposures. Large circles represent Ni atoms, and small circles represent O atoms.

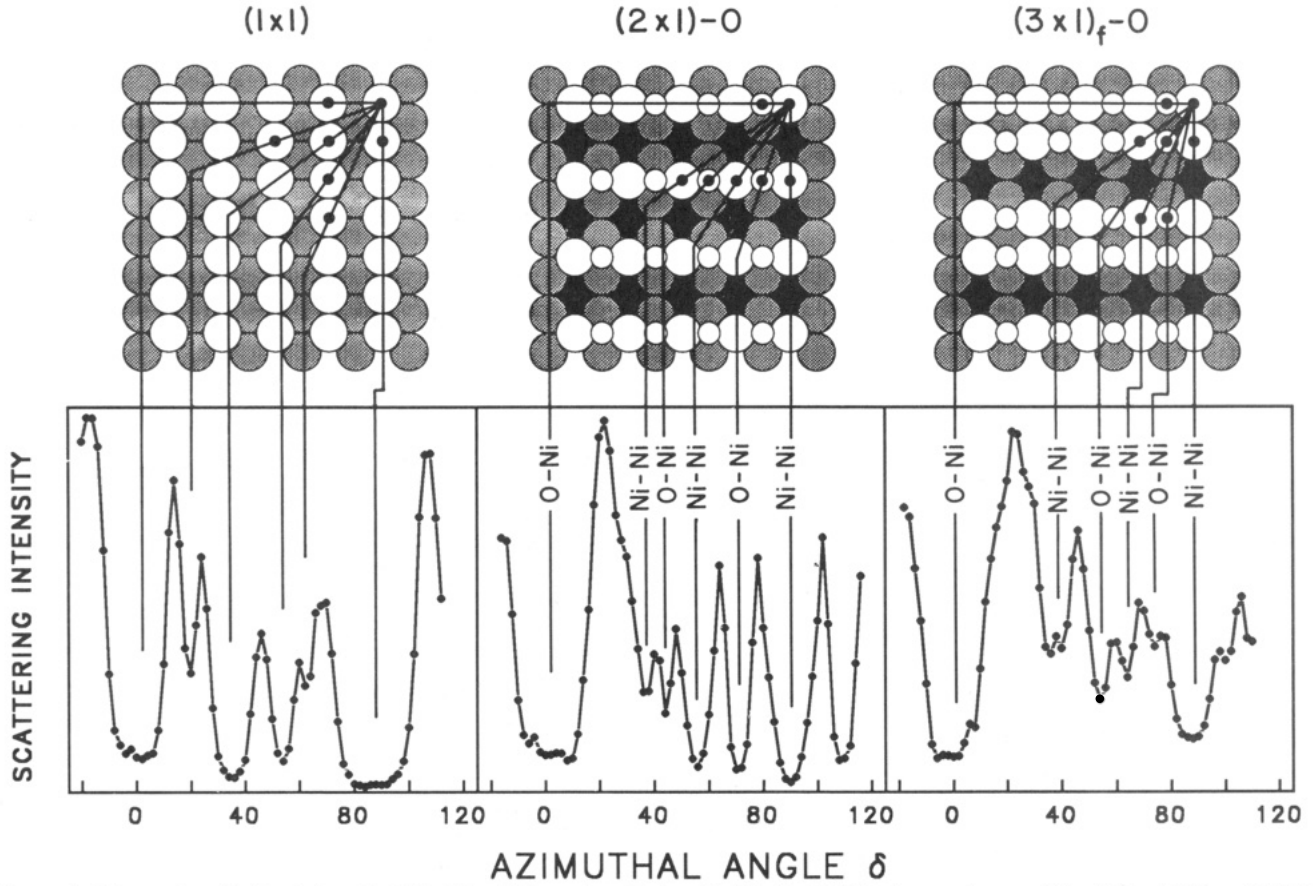

Figure 5. Forward scattering intensity $I(S)$ at $\theta = 30°$ vs azimuthal angle δ for the (1×1) phase using $\alpha = 6°$ and the (2×1) and $(3\times1)_f$ phase using $\alpha = 4.5°$.

⟨1$\bar{1}$0⟩ ($\delta = 90°$) azimuth, indicating that the $(3\times1)_f$ phase has average first-layer spacings between the ⟨001⟩ rows which are intermediate between those of the other two phases.

Structure as a Function of Oxygen Dose. Changes in the surface structure as a function of O_2 dose can be directly observed by monitoring $I(S)$ at $\alpha = 6.5°$ and 13°. The $I(S)$ variations at these two α positions provide a direct measure of the changes in the abundance of $(3\times1)_i$ and (2×1) structures on the surface. The results plotted in Figure 6 show that both structures are initiated at low O_2 exposure and that their $I(S)$ goes through a maximum and then decreases at high dose. The abundance of $(3\times1)_i$ structures maximizes at lower dose than that of the (2×1) structures.

Summary of the Oxygen-Induced Nickel Structure. The TOF-SARS results show that the initial $(3\times1)_i$, (2×1), and final $(3\times1)_f$ substrate phases differ only in the density of the topmost Ni layers as shown in Figure 4; the resulting densities of first-layer Ni atoms are 3.8×10^{14}, 5.7×10^{14}, and 7.6×10^{14} atoms/cm^2, respectively. The densities of the first-layer ⟨001⟩ rows increase with O_2 dose (Figure 6), suggesting that Ni atoms migrate onto terraces where they are stabilized by bonding to O atoms which assume long-bridge sites above these rows.

Sulfur Inhibition of the Oxygen-Induced Reconstruction

The influence of sufur was studied by using a Ni{110} crystal that had 1–3 atom % of a monolayer of sulfur contamination. This concentration was determined by Auger electron spectroscopy (AES). Since the sulfur

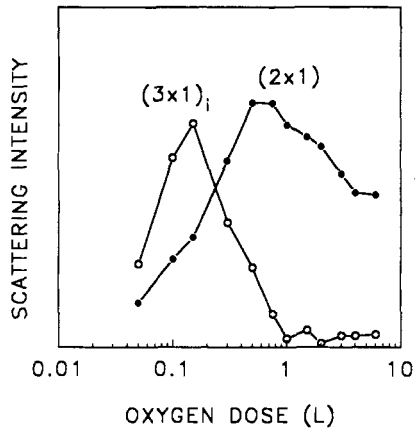

Figure 6. Backscattering intensity $I(S)$ at $\alpha = 6°$ and 13° along $\langle 1\bar{1}0 \rangle$ vs the O_2 exposure dose. $I(S)$ at these α positions is proportional to the abundance of the $(3\times1)_i$ phase at 6° and the (2×1) phase at $\alpha = 13°$.

LMM Auger electrons that were monitored have an escape depth of ≈8 Å, i.e, ≈6 atomic layers, the distribution of the sulfur within these layers is not known. Despite this impurity, the sample exhibited a sharp (1 × 1) LEED pattern and a sharp (2×1) pattern following O_2 dosing at 0.75 langmuir, indicating that the long-range order of the Ni structure was preserved.

Influence of Sulfur on Nickel Periodicity. Azimuthal angle δ scans on clean and sulfur-contaminated (1×1) and (2×1) surfaces[24] are shown in Figure 7. The scans for both samples in the (1×1) unreconstructed phase are very similar. The fact that the positions of all of the minima are reproduced on the sulfur-contaminated surface indicates that (i) the outermost Ni layer has the same structure in both cases and (ii) S atoms are not causing a noticeable perturbation on the Ne trajectories due to their low concentration. For the (2×1) reconstructed phase, the scans differ greatly. For the sulfur-contaminated surface, the sharp maxima and minima in the region $30° < \delta < 100°$ are obliterated and the region becomes featureless, although the deep minimum at $\delta = 0°$ remains unchanged from that of the clean surface. This indicates that the reconstruction is incomplete in the following manner. The featureless region for $\delta > 30°$ indicates that the short-range order is seriously disturbed, i.e., the individual interatomic spacings are irregular, along these directions. The persistence of the deep minimum at $\delta = 0°$ indicates that the structure is well ordered along the $\langle 001 \rangle$ direction; i.e., there are long $\langle 001 \rangle$ rows with O atoms in the bridge positions above these rows. Note that the $\delta = 0°$ minima for the (2×1) phase are broader and deeper than those of the (1×1) phase. This is due to the position of the O atoms; azimuths with short interatomic spacings require larger δ rotations for neighboring atoms to move out of the shadow cones. This indicates that the O atoms reside in the long-bridge sites on the S-contaminated surface as well as the clean surface.

Influence of Sulfur on Nickel Interatomic Spacings. Incident angle α scans on the clean and sulfur-contaminated (1×1) and (2×1) surfaces[24] are shown in Figure 8. The scans for both samples in the (1×1) unreconstructed phase are very similar, indicating that the contaminant does not cause a significant perturbation of the Ni interatomic spacings. For the (2×1) reconstructed phase, the scans are significantly different for the two samples. These differences are as follows: (i) Different α_c values are observed along the $\langle 1\bar{1}0 \rangle$ direction (Figure 8c) and (ii) only intensity variations are observed along the $\langle 001 \rangle$ direction (Figure 8d). Result i indicates that the Ni interatomic spacings are changed along $\langle 1\bar{1}0 \rangle$. The lower α_c value for the sulfur-contaminated surface shows that some of its first-layer spacings are longer than those of the uncontaminated sample. Referring to Figures 8c and 3B, the uncontaminated sample exhibits $\alpha_c = 9.8°$, which corresponds to $d = 5.0$ Å, in good agreement with a doubling of the lattice constant, i.e., $2d(\langle 1\bar{1}0 \rangle) = 4.98$ Å. The scan for the contaminated sample exhibits two distinct values at $\alpha_c = 7.2°$ and 15.5°, which corresponds to $d = 7.5$ and 2.6 Å, respectively, or $3d(\langle 1\bar{1}0 \rangle) = 7.47$ Å and $d(\langle 1\bar{1}0 \rangle) = 2.49$ Å. It is not possible to assess the contributions from the $2d(\langle 1\bar{1}0 \rangle)$ spacings, since this edge would occur at $\alpha_c \approx 10°$, where it is overlapped on both sides by the $3d$ and d contributions. Result ii indicates that the outermost interlayer spacings are different in the two samples. The three peaks in Figure 8d correspond to first-layer atoms shadowing neighboring first-layer atoms (surface scattering) for the 15° peak and nth-layer atoms shadowing $(n + 2)$-layer atoms (subsurface scattering) for the 25° and 45° peaks, where $n = 1$, 2, and 3. The enhancement of subsurface scattering in the S-contaminated sample indicates an expansion of the interlayer spacing.

Summary of Results on the Influence of Sulfur on the Nickel Structure. The TOF-SARS data are consistent with a model for the S-contaminated surface in which the $\langle 001 \rangle$ rows are formed; however, the distances between these rows along the $\langle 1\bar{1}0 \rangle$ direction are irregular. The persistence of a sharp LEED pattern indicates that there are long-range (>200 Å) ordered domains; however, the short-range (individual interatomic spacings) order is disturbed within these domains.

Atomic Scale Mechanisms

Oxygen-Induced "Added Row" Reconstruction of Nickel. The observations that the interatomic spacings along the $\langle 1\bar{1}0 \rangle$ direction decrease from $3d$ to $2d$ and then to a combination of $(2d + d)$ as a function of increasing O_2 exposure are consistent with an "added row" reconstruction mechanism.[25] In such a mechanism, Ni atoms migrate from step edges and imperfections onto terraces. Oxygen atoms originating from dissociative chemisorption of O_2 are also mobile on these terraces. These Ni and O atoms diffuse over the terraces until they encounter each other. The strongly attractive Ni–O interactions result in the formation of chains of Ni atoms along $\langle 001 \rangle$ on top of the terraces. These chains are held together by bonding to the O atoms which are situated in the long-bridge positions above the rows. The density of these $\langle 001 \rangle$ rows increases along the $\langle 1\bar{1}0 \rangle$ direction as the amount of available adsorbed O atoms increases.

Sulfur Inhibition of the Oxygen-Induced Reconstruction. The observations on the S-contaminated surface that (i) the $\langle 001 \rangle$ Ni rows are still formed and (ii) the O atoms still occupy the same long-bridge sites

(25) Coulman, D. J.; Wintterlin, J.; Behm, R. J.; Ertl, G. *Phys. Rev. Lett.* **1990**, *64*, 1761. Jensen, F.; Besenbacher, F.; Laesgaard, E.; Stensgaard, I. *Phys. Rev. B.* **1990**, *41*, 10233. Kuk, Y.; Chua, F. M.; Silverman, P. J.; Meyer, J. A. *Phys. Rev. B.* **1990**, *41*, 12393. Jacobsen, K. W.; Norskov, J. K. *Phys. Rev. Lett.* **1990**, *65*, 1788.

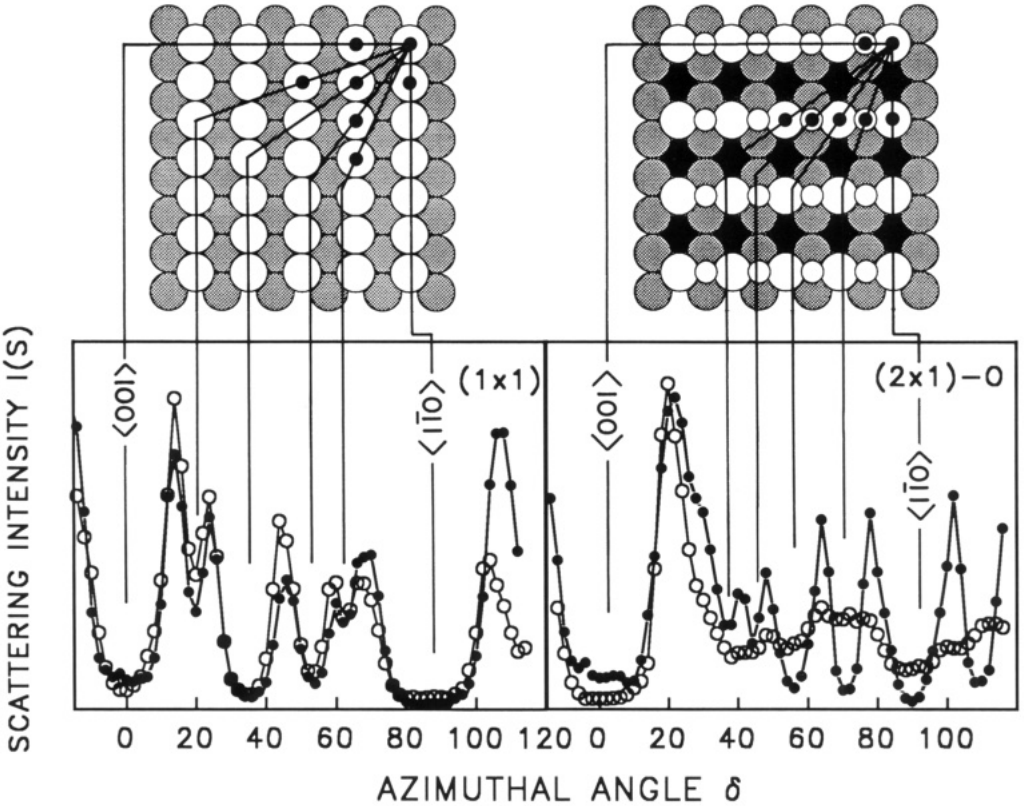

Figure 7. Scattering intensity $I(S)$ vs azimuthal angle δ for Ni{110} in the (1×1) and (2×1)-O phases. The solid points are from a clean Ni sample, and the open points are from a sulfur-contaminated Ni sample. Conditions: 4-keV Ne^+; scattering angle $\theta = 30°$; incident angles $\alpha = 6°$ for (1×1) and $\alpha = 4.5°$ for (2×1)-O.

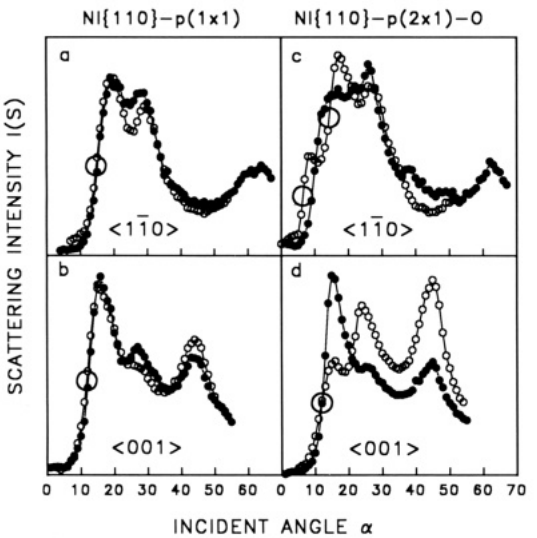

Figure 8. Scattering intensity $I(S)$ vs incident angle α along the $\langle 1\bar{1}0\rangle$ and $\langle 001\rangle$ azimuths for Ni{110} in the (1×1) and (2×1)-O phases. The solid points are from a clean Ni sample and the open points are from a sulfur contaminated Ni sample. Conditions: 4-keV Ne^+; scattering angle $\theta = 90°$.

on these rows, but (iii) the distances between these rows along the $\langle 1\bar{1}0\rangle$ direction vary, indicate that the presence of S atoms inhibits the complete surface reconstruction. It has been determined previously[16] that S atoms on a Ni{110} surface occupy 4-fold hollow sites in which S is bonded to one Ni atom in the second-layer and four Ni atoms in the first-layer. The presence of S induces an expansion of the first- to second-layer spacing by 6–10%. This expansion is believed to be caused by the tendency of the Ni surface atoms to make a planar arrangement with the S atom, which can only be achieved by lifting the Ni surface atoms, since S is already directly on top of a second-layer Ni atom. The most energetically favorable diffusion path for Ni atoms migrating on the terraces is along the $\langle 1\bar{1}0\rangle$ direction, as has been observed[25] for Cu atoms on a Cu{110} surface. This path will take the Ni atoms directly over the 4-fold hollow surface sites and, hence, the contaminant S atoms. Such a path evidently presents a considerable kinetic barrier to the diffusing Ni atoms, i.e., the S atoms block the diffusion path of the Ni atoms.

Atomistic Model. An atomistic model of the formation of the Ni{110}-(2×1)-O phase is shown in Figure 9. Ni atoms diffuse from the step edge of the (1×1) terrace on the left side onto the lower terrace on the right side. The $\langle 001\rangle$ Ni–O chains on the right side are formed as a result of interaction of Ni and O atoms on this lower terrace. The S atoms block the diffusion paths of the Ni atoms along the $\langle 1\bar{1}0\rangle$ direction, resulting in irregular spacings between the Ni–O chains.

Consider the following simplified thermodynamic scheme to illustrate the bond energy changes upon chemisorption. The average Ni–Ni bond energy (E_{Ni-Ni}) for Ni atoms on the {110} surface can be approximated as the enthalpy of sublimation divided by the number of nearest neighbors (7) in the surface, i.e., $E_{Ni-Ni} = (4.4\ eV)/7 = 0.63\ eV/bond$. The Ni–O bond energy ($E_{Ni-O}$) can be approximated as one-half the enthalpy of adsorption of O_2, i.e., $E_{Ni-O} = 5.2\ eV/2 = 2.6\ eV/bond$. A Ni atom in an oxygen-stablized $\langle 001\rangle$ chain is bound to five other Ni atoms and two O atoms. Thus, the net energy gain in forming the Ni–O $\langle 001\rangle$ chains can be estimated as $\Delta E \approx 2(E_{Ni-O} - E_{Ni-Ni}) = 3.9\ eV/Ni\ atom$.

The driving force behind the reconstruction or mass transport of Ni is due to the greater stability of the

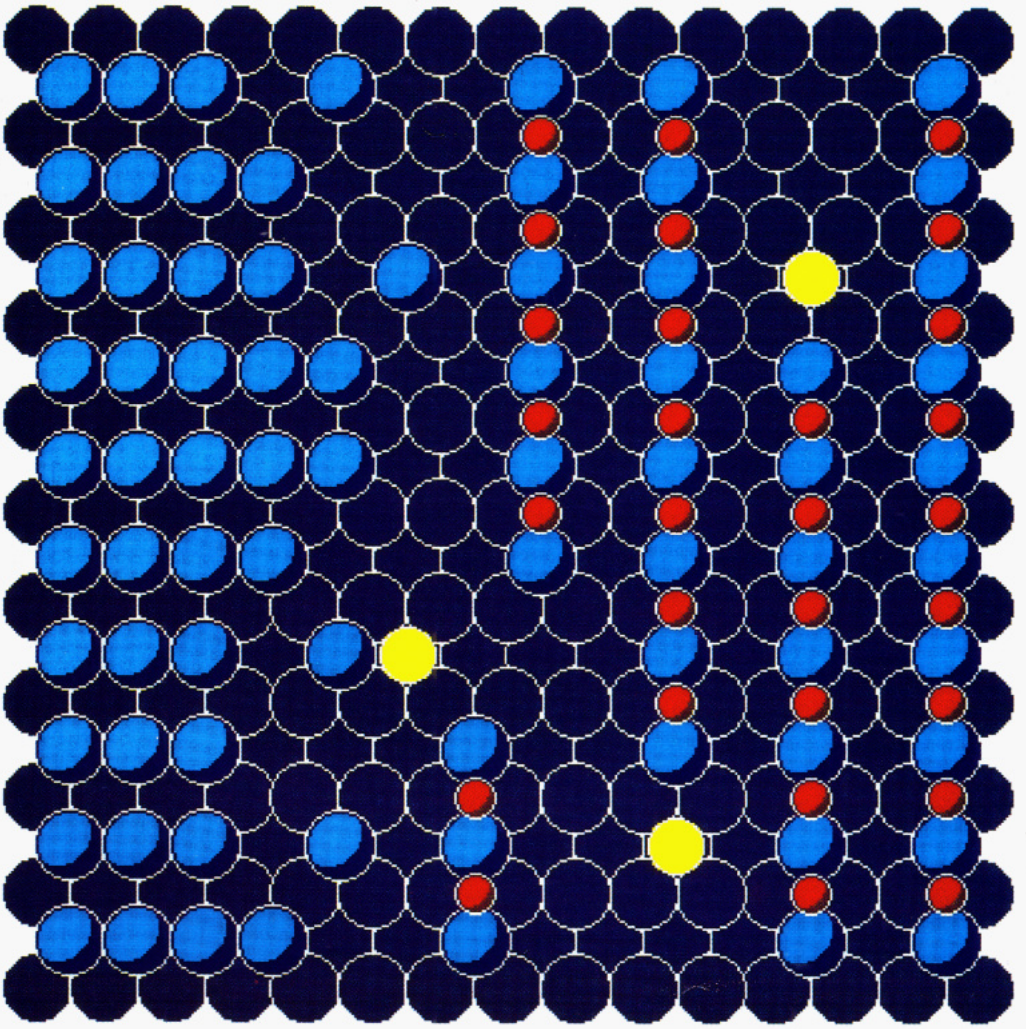

Figure 9. Atomistic model of a surface vicinal to the Ni{110} surface illustrating O atom (red) induced and S atom (yellow) inhibition of the Ni atom (light blue, surface layer; dark blue, subsurface layers) reconstruction. The left side of the diagram shows a (1×1) Ni terrace with a jagged step down to another (1×1) Ni terrace. Ni atoms migrate to the right along ⟨1$\bar{1}$0⟩ channels, encountering equally mobile O atoms from dissociative O_2 chemisorption, resulting in formation of stable Ni–O rows along ⟨001⟩ as shown on the right side. Impurity S atoms, situated at the Ni 4-fold hollow sites, present a barrier to the diffusing Ni atoms, resulting in ⟨001⟩ rows with irregular lengths and inter-row spacings.

(2×1)-O phase over a phase in which oxygen is chemisorbed on the existing (1×1) terraces. As an example, the latter phase could consist of O atoms chemisorbed at similar long-bridge sites above every other Ni ⟨001⟩ row of the (1×1) terrace. A Ni atom in such a surface phase would be bound to seven other Ni atoms as well as two O atoms. The Ni–O bond is a highly localized, directional bond compared to the delocalized, metallic nature of the Ni–Ni bonds. The formation of such Ni–O bonds requires a rehybridization of the Ni 3d atomic orbitals for covalent bonding to the O 2p atomic orbitals. This rehybridization is, evidently, incompatible with Ni–Ni bonding along the ⟨1$\bar{1}$0⟩ direction where there are two close Ni neighbors in the (1×1) phase, resulting in an unstable configuration. Electronic structure calculations would be necessary to unravel these details.

Concluding Remarks

It is apparent that solid surfaces are by no means static, i.e., the surface atoms of a metal are highly mobile even at room temperature. This mobility is crucial to the formation of adsorbate structures and the inhibition of these processes. Specifically, it is found that 1–3 atom % of sulfur on a Ni{110} surface is capable of inhibiting the oxygen-induced reconstruction to such an extent that the surface short-range order is seriously disturbed and the oxidation is incomplete. The sulfur impurity blocks the diffusion of Ni atoms in the "added-row" reconstruction. Thus, the thermodynamic driving force for formation of the Ni{110}-(2×1)-O phase is limited by the kinetic barrier for diffusion of Ni atoms over the sulfur-contaminated surface. Macroscopic phenomena, such as surface chemical reactions, catalysis, and inhibition of catalytic activity, consist of a series of elementary atomic steps. Understanding a macroscopic phenomenon in terms of theories derived from first principles requires a knowledge of these elementary atomic processes. It is in the investigation of the mechanisms of these elementary atomic processes that modern surface analysis techniques find their most useful applications.

This material is based on work supported by the National Science Foundation under Grant No. CHE-8814337, the R. A. Welch Foundation under Grant No. E-656, and the Texas Advanced Research Program under Grant No. 3652022ARP.